MAGNETOHYDRODYNAMICS Vol. 58 (2022), No. 3, pp. 339–347
DOI: 10.22364/mhd.58.3.9

EFFECT OF VISCOSITY ON TORNADO-LIKE FLOW DRIVEN BY A SPINNING MAGNET

Ilmārs Grants

Institute of Physics, University of Latvia, 32 Miera str., LV-2169 Salaspils, Latvia

Tornado-like flow is created by a cylindrical transversely magnetized permanent magnet rotating co-axially below a conducting liquid cylinder. Several geometries are considered numerically, with a focus on the low-Reynolds number regime. The effect of viscosity is discussed in terms of dimensional analysis. The increased viscosity decreases the maximum swirl just slightly as long as the flow remains dominated by inertia. The secondary downdraft slightly increases with the viscosity in this regime, reaching a maximum at the dimensionless electromagnetic torque value around 2×10^4 in all considered geometries. The maximum is accompanied by a vortex breakdown flow. The downdraft velocity decreases rapidly with the viscosity after the maximum. The respective optimum viscosity is shown to increase proportionally to the setup size provided that the skin-effect becomes significant.

Introduction.

Rotating permanent magnets (PM) offer a wide range of contactless stirring options for liquid metals. There is one configuration which appears particularly encouraging for the purpose of stirring reinforcement particles into the melt (configuration A in [1]). This configuration features a magnetic dipole with magnetization in the horizontal plane placed under the crucible. When the dipole rotates around the vertical axis, an electromagnetic body force is induced [1] in a narrow layer at the crucible's bottom. This body force creates [1] a tornado-like flow akin of the rotating magnetic bar driven flow in the laboratory stirrer [2]. Being sufficiently intense, the flow features a narrow vortex funnel at the top surface and a rapid downdraft near the axis. The flow is also most turbulent near the top surface. These flow features apparently provide perfect conditions for particles being submerged into the melt. This alone, however, is not necessarily enough for particles to remain in the metal. If they are not well wetted by the metal, then after submersion they tend to accumulate at the crucible wall – the first solid surface encountered [3]. A semi-solid metal slurry provides a multitude of tiny internal solid surfaces for particles to stick at. This may explain the success of compo-casting [4], whereby the ceramic particles are mechanically stirred into a semi-solid metal slurry. The rotating PM could replace the mechanical stirrer with a contactless "electromagnetic tornado". Though there is a potentially formidable obstacle. The viscosity of the semi-solid alloy increases significantly compared to the fully molten state. At some point the electromagnetic stirring should become ineffective. This study addresses the corresponding condition in terms of the effective viscosity. Besides, the study is also concerned with the effects of magnet–melt separation and melt–magnet size ratio on the performance of a PM stirrer.

1. Formulation.

Suppose that the melt temperature is equal everywhere in the crucible and close to liquidus so that the melt remains a Newtonian fluid. As a first approximation, it is assumed that all effects of the solidified fraction may be captured by an increased effective viscosity being constant in the entire volume. It is supposed additionally that

the metal is covered by a solid lid preventing surface deformation. The reinforcement particles are supposed to form a relatively thin layer under the lid. The action of the rotating PM is modelled by a time-averaged electromagnetic force [5] which has only the azimuthal component. This force is assumed to be flow independent at a low magnetic Reynolds number and a negligible magnetic field slip (i.e. when the PM rotates much faster than the fluid).

1.1. Equations. The Navier–Stokes equation is solved for an incompressible flow in a cylinder in dimensionless form

$$\frac{\partial \mathbf{v}}{\partial t} + (\nabla \times \mathbf{v}) \times \mathbf{v} = \nabla^2 \mathbf{v} - \nabla P + \mathrm{Ta}\, f(r,z)\mathbf{e}_\phi, \tag{1}$$

$$\nabla \cdot \mathbf{v} = 0, \tag{2}$$

for the velocity $\mathbf{v}$ and pressure P with the cylinder half-height H_0, momentum diffusion time H_0^2/ν and ρH_0^3 as the distance, time and mass units, respectively (ν is the effective kinematic viscosity of the melt and ρ is the density). The no-slip boundary conditions $\mathbf{v} = 0$ are applied for the velocity at all surfaces of the cylinder. The electromagnetic body force magnitude is characterized by the magnetic Taylor number

$$\mathrm{Ta} = \frac{\sigma \omega B_\mathrm{R}^2 H_0^4}{2\rho\nu^2}, \tag{3}$$

where σ is the conductivity of the melt, ω is the magnet rotation rate, and B_R is its remanent magnetization. The force distribution is described by the dimensionless shape function $f(r,z)$. An analytical solution [5] is available for $f(r,z)$ for a finite-sized cylindrical rotating PM placed co-axially with the cylindrical conductor. Alternatively, $f(r,z)$ may be calculated by time-averaging the numerical solution [1] for the induced currents due to the prescribed alternating magnetic field. Details of the PM and crucible arrangement may diminish the relevance of Eq. (3). Instead, a related dimensionless quantity based on the total electromagnetic torque M may be more appropriate

$$\mathrm{Ta}_M = \mathrm{Ta} \int_V f(r,z) r \mathrm{d}V = \frac{M}{\rho\nu^2 H_0}. \tag{4}$$

1.2. Relation to dimensional quantities. Suppose that all parameters in Eq. (3) are fixed except for the kinematic viscosity. The latter is expressed from Ta as

$$\nu = H_0^2 \sqrt{\frac{\sigma\omega B_\mathrm{R}^2}{2\rho}}\, \mathrm{Ta}^{-1/2}. \tag{5}$$

The dimensional flow velocity $\mathbf{v}^*$ is expressed from its dimensionless counterpart $\mathbf{v}$, the solution of Eqs. (1),(2), by multiplying with the velocity scale

$$\mathbf{v}^* = \frac{\nu}{H_0}\mathbf{v} = H_0 \sqrt{\frac{\sigma\omega B_\mathrm{R}^2}{2\rho}}\, \mathrm{Ta}^{-1/2}\mathbf{v}. \tag{6}$$

It becomes evident from this expression that the flow velocity $|\mathbf{v}^*|$ is independent of viscosity if $|\mathbf{v}| = O(\mathrm{Ta}^{1/2})$. Such correlation was in close agreement with the numerical results of [1]. These results, however, did not cover transition towards the Stokes regime.

Table 1. The properties of metal and permanent magnet (PM).

	symbol	value
conductivity	σ	2×10^6 S/m
density	ρ	2600 kg/m^3
PM rotation rate	ω	2000 rad/s
radius	R_m	0.02 m

Filling this gap is one of the tasks for the current study. This is done in dimensionless terms and using also a specific example with the liquid and PM properties summarized in Table 1. The liquid properties are chosen to approximate typical values in aluminium melts. The magnet rotation rate is rounded off from what has been proven feasible (400 Hz) in a laboratory test with a 40 mm diameter magnet.

2. Numerical techniques.

The freely available three-dimensional time-dependent spectral hydrodynamic simulation program package `c3dt` [1, 6] was used with a time-averaged electromagnetic body force as the source of motion. The time-averaged three-dimensional flow was computed in the unstable flow regime. In case of a higher viscosity (lower Ta), where the flow was stable, the axially symmetric stationary solution was obtained by advancing Eqs. (1),(2) in time. The function $f(r, z)$ was computed numerically using `c3dt` by time-averaging the numerical solution for the electromagnetic force term over one PM rotation period. The electromagnetic force computations were cross-checked by the analytical solution [5] in terms of the integral torque (4). The numerically calculated value of the ratio $\mathrm{Ta}_M/\mathrm{Ta}$ was 1.6653×10^{-3} for the geometry displayed in Fig. 1*b*, while the analytical solution produced 1.6649×10^{-3} (the difference less than 0.025%).

The spatial resolution was 49 and 43 modes in the z- and r-directions, respectively, for cases with a stable axially symmetric flow. The three-dimensional unstable flow resolution varied from $65 \times 49 \times 25$ to $85 \times 49 \times 49$ to 85^3 to 97^3 for $\mathrm{Ta} = 3 \times 10^7$,$10^8$, 3×10^8, and 10^9, respectively. The time step was between 10^{-7} and 10^{-3} depending on Ta. The unstable flow was averaged over 10^5 time steps.

3. Results.

Four configurations have been considered with the melt geometry fixed (diameter equal to height). The basic configuration had a 40×40 mm magnet in combination with a 46 mm inner diameter crucible at the $h = 10$ mm distance from the magnet (Fig. 1). The second and the third configuration considered the same magnet below a larger 80 mm or 140 mm inner diameter crucible at the same 10 mm distance. Finally, the already computed results of [1] for the idealized magnetic dipole have been supplemented with the data for lower Ta_M. The magnet–metal separation of 10 mm was selected after a round of certain "optimization", where the electromagnetic torque was computed as a function of the magnet–melt distance h. The results of this computation are displayed in Fig. 2 (assuming the conditions of Table 1). The driving torque almost doubled by halving the distance h to 5 mm. Although marginally feasible, this would be an expensive endeavor because of the technical difficulties to cool the magnet. When the distance was doubled to $h = 20$ mm, the computed torque decreased more than three-fold. Thus, the torque decreased somewhat faster than inversely proportional to h when the separation h was more than 10 mm (half of the magnet radius).

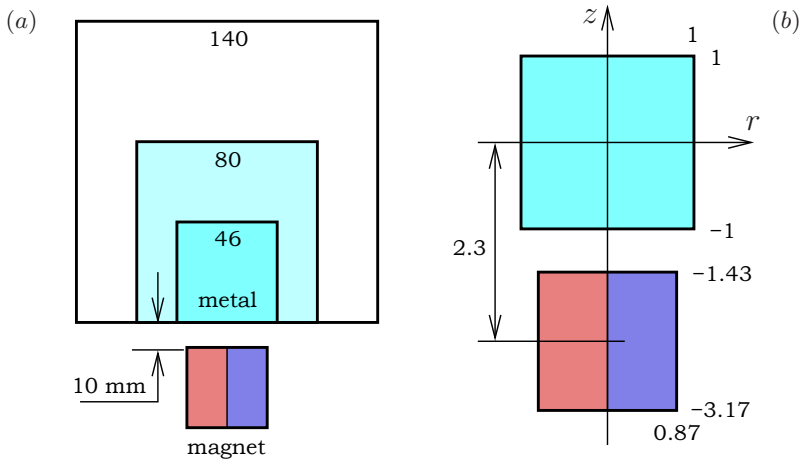

Fig. 1. (*a*) Schematic presentation of the magnet and crucible location in three basic configurations. (*b*) The dimensionless geometry model for a 46 mm crucible.

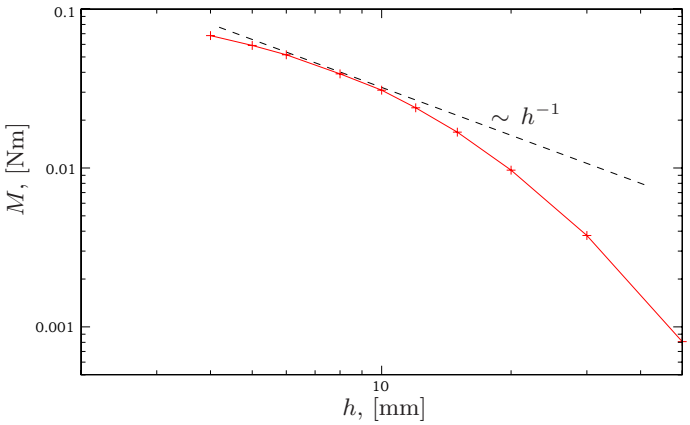

Fig. 2. Electromagnetic torque as a function of the magnet–metal separation under the conditions of Table 1 and $H_0 = 0.023$ m.

Fig. 3*a* displays the maximum downdraft speed and the maximum azimuthal velocity as a function of Ta_M in three magnet configurations. In all cases a "bump" in the axial velocity dependence was observed at $\mathrm{Ta}_M \approx 2 \times 10^4$. The maximum azimuthal velocity dependences were comparably smooth and nearly overlapping in all four cases. The downdraft speed, in turn, varied considerably between the configurations. Fig. 3*b* displays the same data in terms of dimensional velocities vs. kinematic viscosity under the conditions of Table 1. The downdraft speed initially increased as the viscosity increased from the minimum considered value, whereas the azimuthal velocity decreased monotonically. Note that the dash-dotted line displaying $O(\mathrm{Ta}^{1/2})$ slope in Fig. 3*a* corresponds to a viscosity-independent velocity. Such property was observed for the maximum downdraft speed at a low viscosity in Fig. 3*b*.

The aforementioned "bump" occurred as the flow underwent a vortex breakdown marked by characteristic changes in the velocity distribution [7, 8]. The axial and azimuthal velocity distributions for the selected Ta_M values are displayed in Figs. 4 and 5.

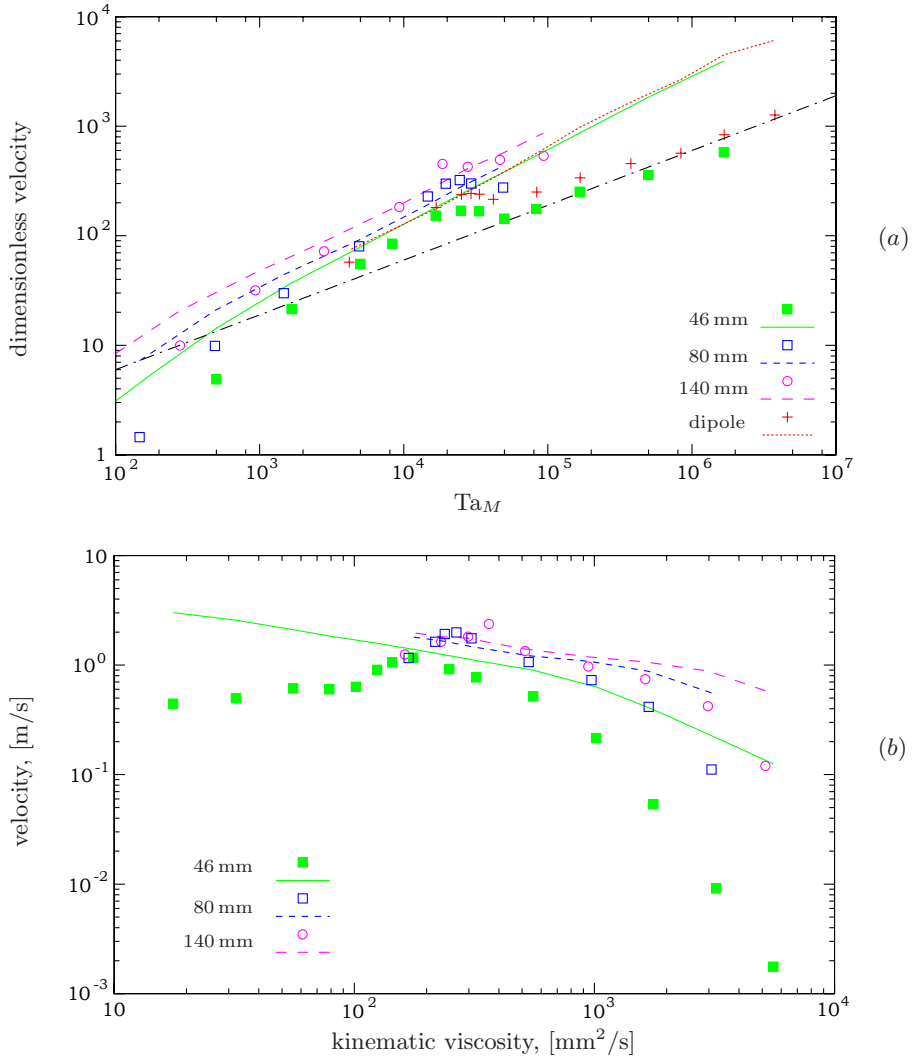

Fig. 3. Dimensionless velocity–torque dependence (a) and equivalent velocity–viscosity dependence (b) under the conditions of Table 1 and variable crucible dimensions. The maximum downdraft speed and maximum azimuthal velocity are displayed by points and lines, respectively. The dash-dotted line in (a) displays a $O(\mathrm{Ta}_M^{1/2})$ slope.

The middle plot in these figures corresponds approximately to the vortex breakdown. Fig. 6 displays vertical velocity profiles at the axis under the same conditions as in Fig. 4. The initial increase of the maximum downdraft speed with the viscosity was accompanied by a slight decrease of the profile steepness near the top surface ($z = 1$). The latter characteristic might be even more consequential for the particle entrainment than the maximum downdraft speed. If so, then increasing viscosity would not improve conditions as much as Fig. 4 might seem to suggest. Yet, the profile steepness was little affected up to the vortex breakdown (bold curve). Thus, the computations give no reason to expect

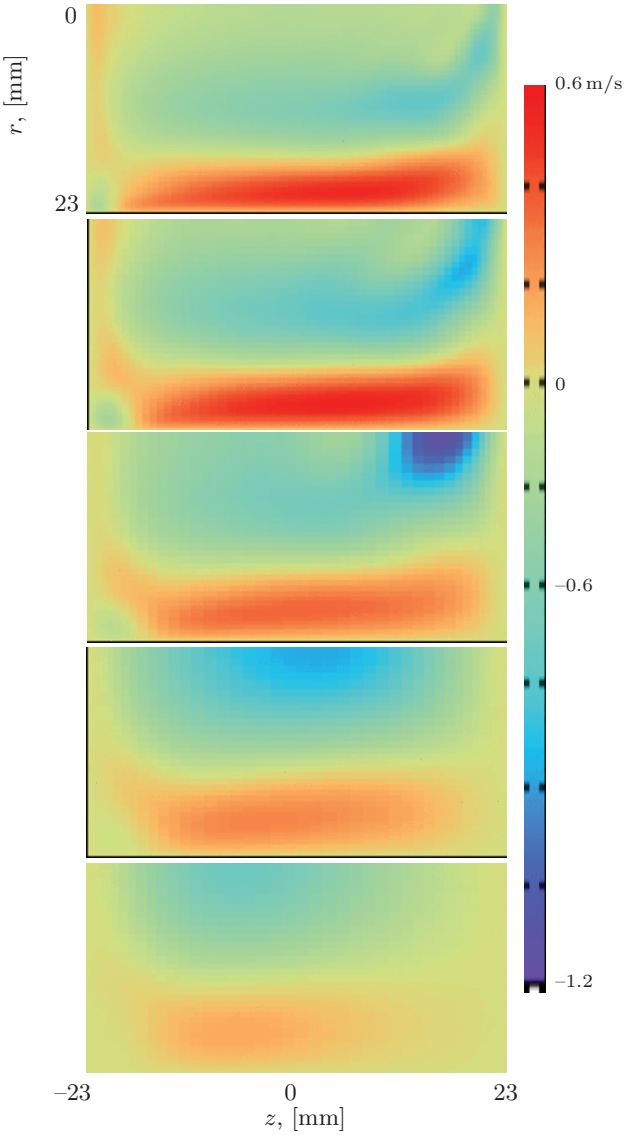

Fig. 4. Axial velocity distributions in the 46-mm crucible under the conditions of Table 1 at $\mathrm{Ta}_M = 1.67 \times 10^5, 0.5 \times 10^5, 1.67 \times 10^4, 5000, 1670$ or viscosity $\eta = 0.15$, 0.26, 0.46, 0.84, 1.5 Pa·s from top to bottom, respectively.

adverse effects of the increased viscosity in this range. Any similarity to tornado all but disappeared as the viscosity increased significantly past the vortex breakdown optimum (bottom plots in Figs. 4 and 5). Such flow pattern would unlikely be useful for particle entrainment from the top even at a high maximum speed. A fixed geometry flow has been considered in this study assuming a rigid lid at the top. Expectedly, the upper free surface would deform strongly under the stirring conditions of Table 1. It is not immediatelly clear whether surface deformation may aid the particle entrainment. Although it is quite certain that the numerical complexiy of the problem would grow significantly. It

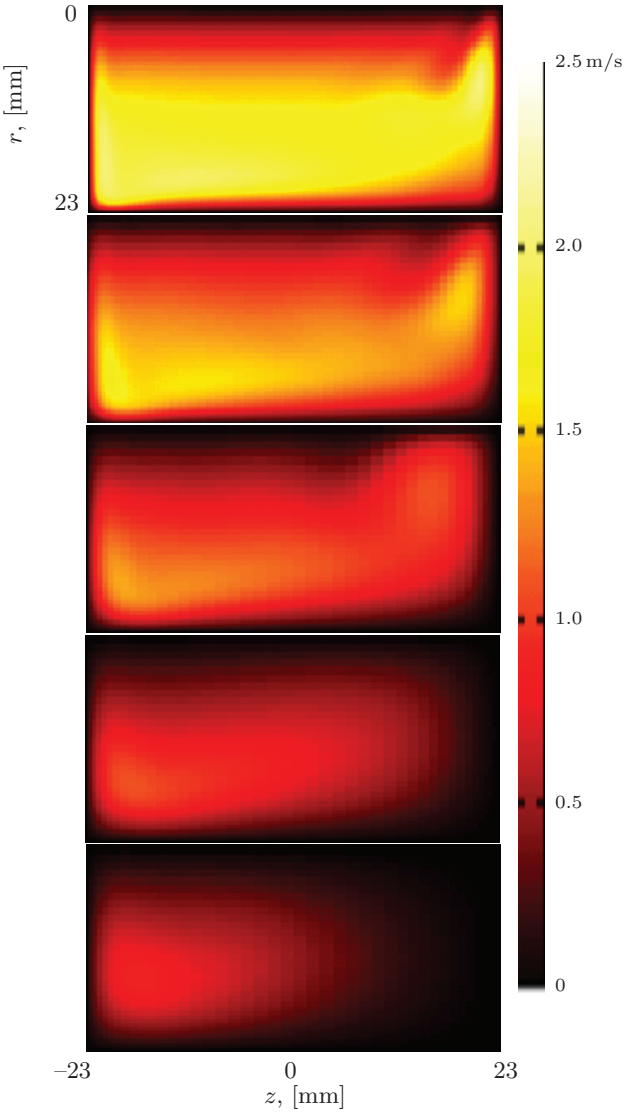

Fig. 5. Azimuthal velocity distributions in the 46-mm crucible under the conditions of Table 1 at $\mathrm{Ta}_M = 1.67 \times 10^5, 0.5 \times 10^5, 1.67 \times 10^4, 5000, 1670$ or viscosity $\eta = 0.15$, 0.26, 0.46, 0.84, 1.5 Pa·s from top to bottom, respectively.

is, therefore, reasonable to proceed with an experimental test, where both options could be compared with a little additional effort. The lid could be placed on a layer of floating particles just before turning the PM rotation on. To prevent co-rotation of the lid, a blocking protrusion may be needed on it.

Finally, let us consider consequences of the up-scaling. The condition of the vortex breakdown in all considered configurations was approximated by $\mathrm{Ta}_M \approx 2 \times 10^4$ (Fig. 3). With all other parameters being fixed, the magnetic torque M scales with the setup size characterized below by the magnet radius R_m and frequency ω as $M = O(\omega R_\mathrm{m}^5)$. In the case of a relevant skin-effect, the frequency is constrained to $\omega = O(R_\mathrm{m}^{-2})$, producing

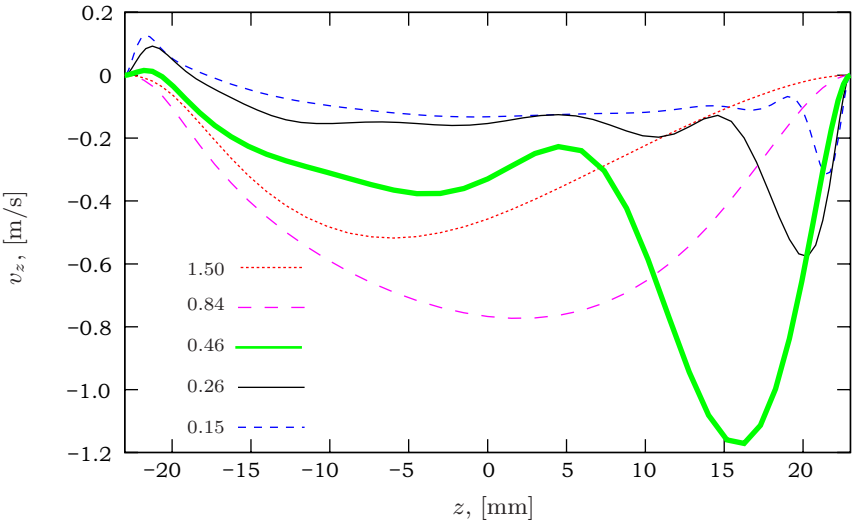

Fig. 6. Axial velocity profiles at the axis for the variable effective viscosity as in Fig. 4.

$M = O(R_{\rm m}^3)$. Substituting this into Eq. (4) for $\mathrm{Ta}_M \approx 2\times10^4$ and invoking $H_0 = O(R_{\rm m})$ yield scaling of the optimum kinematic viscosity,

$$\nu_c \approx 0.01\sqrt{\frac{M}{2\rho H_0}} = O(R_{\rm m}). \tag{7}$$

Accordingly, the optimum viscosity increases in proportion to the setup size when the driving torque is limited by the skin-effect. Otherwise, provided also that the frequency can be maintained constant, the optimum viscosity increases proportionally to the square of the setup size. These results suggest that better stirring results may be reasonably expected in larger crucibles. However, it is not necessary to increase the size of the magnet at the same time. On the contrary, a higher downdraft speed and a higher threshold viscosity were observed in comparably larger crucibles (Fig. 3*b*). Thus, the choice of the magnet size is mostly determined by the thickness of the crucible wall.

4. Conclusions.

- The magnet–metal separation should not exceed the half of the magnet radius as the electromagnetic driving torque decreases rapidly with a larger separation.
- The primary swirl slightly decreases with the increasing viscosity, whereas the downdraft speed slightly increases with the increasing viscosity up to the onset of the vortex breakdown at ν_c that corresponds to $\mathrm{Ta}_M \approx 2\times10^4$. At a yet higher viscosity a rapid decrease of the downdraft speed follows.
- In a small laboratory experiment in a 46-mm diameter crucible the threshold viscosity may be as high as about 0.5 Pa·s for semi-solid aluminum alloys (comparable to the viscosity of motor oil).

- The threshold viscosity increases in proportion (at least) to the setup size under up-scaling.
- When the crucible is considerably larger than the magnet, the downdraft speed may exceed the primary swirl.

Acknowledgements.
This study was financed by the European Regional Development Fund under grant no. 1.1.1.1/19/A/080. The analytical value of the dimensionless magnetic torque in Section 2 was provided by Didzis Berenis.

References

[1] I. Grants. Rotating magnetic dipole-driven flows in a conducting liquid cylinder. *J. Phys. Fluids*, vol. 33 (2021), 055115; DOI: 10.1063/5.0047240.

[2] G. Halász, B. Gyüre, I.M. Jánosi, K. G. Szabó, and T. Tél. Vortex flow generated by a magnetic stirrer. *American J. Phys.*, vol. 75 (2007), 1092–1098; DOI: 10.1119/1.2772287.

[3] I. Grants, D. Räbiger, T. Voght, S. Eckert, G. Gerbeth. Application of magnetically driven tornado-like vortex for stirring floating particles into liquid metal. *Magnetohydrodynamics*, vol. 51 (2015), 3, 419–424; DOI: 10.22364/mhd.51.3.2

[4] A. Mazahery and M.O. Shabani. Microstructural and abrasive wear properties of SiC reinforced aluminum-based composite produced by compocasting. *Trans. Nonferrous Met. Soc. China*, vol. 23 (2013), 1905–1914.

[5] D. Berenis and I. Grants. Analytical induced force solution in conducting cylindrical bodies and rings due to a rotating finite permanent magnet. *J. Magnetism and Magn. Mat.*, vol. 497 (2020), 165856.

[6] I. Grants. Source code of spectral numerical solver for incompressible time-dependent 3D Navier–Stokes equation in cylinder in alternating and/or static external magnetic fields. *Reserchgate*, (2021); DOI: 10.13140/RG.2.2.22879.18081.

[7] M.P. Escudier. Observations of the flow produced in a cylindrical container by a rotating end wall. *Exp. Fluids*, vol. 2 (1984), 189–196; DOI: 10.1007/BF00571864.

[8] A.Yu. Gelfgat, P.Z. Bar-Yoseph, and A. Solan. Three-dimensional instability of axisymmetric flow in a rotating lid–cylinder enclosure. *J. Fluid Mech.,*, vol. 438 (2000), 363–377.

Received 10.10.2022